Title

Exploring the Charge Compensation Mechanism of P2-Type Na0.6Mg0.3Mn0.7O2 Cathode Materials for Advanced Sodium-Ion Batteries

Journal

Energies, 13(21)

ISSN

1996-1073

Authors

Cheng, Chen
Ding, Manling
Yan, Tianran
et al.

Publication Date

2020

DOI

10.3390/en13215729

Peer reviewed

energies

MDPI

Article

Exploring the Charge Compensation Mechanism of P2-Type $Na_{0.6}Mg_{0.3}Mn_{0.7}O_2$ Cathode Materials for Advanced Sodium-Ion Batteries

Chen Cheng [1], Manling Ding [1], Tianran Yan [1], Kehua Dai [2], Jing Mao [3], Nian Zhang [4], Liang Zhang [1,*] and Jinghua Guo [5,6,*]

1 Jiangsu Key Laboratory for Carbon-Based Functional Materials & Devices, Institute of Functional Nano & Soft Materials (FUNSOM), Soochow University, 199 Ren'ai Road, Suzhou 215123, China; 20184214128@stu.suda.edu.cn (C.C.); 20184214029@stu.suda.edu.cn (M.D.); 20194214102@stu.suda.edu.cn (T.Y.)
2 College of Chemistry, Tianjin Normal University, Tianjin 300387, China; Daikh@smm.neu.edu.cn
3 School of Materials Science and Engineering, Zhengzhou University, Zhengzhou 450001, China; maojing@zzu.edu.cn
4 State Key Laboratory of Functional Materials for Informatics, Shanghai Institute of Microsystem and Information Technology, Chinese Academy of Sciences, Shanghai 200050, China; zhangn@mail.sim.ac.cn
5 Advanced Light Source, Lawrence Berkeley National Laboratory, Berkeley, CA 94720, USA
6 Department of Chemistry and Biochemistry, University of California, Santa Cruz, CA 95064, USA
* Correspondence: liangzhang2019@suda.edu.cn (L.Z.); jguo@lbl.gov (J.G.)

Received: 2 September 2020; Accepted: 29 October 2020; Published: 2 November 2020

Abstract: P2-type sodium layered transition metal oxides have been intensively investigated as promising cathode materials for sodium-ion batteries (SIBs) by virtue of their high specific capacity and high operating voltage. However, they suffer from problems of voltage decay, capacity fading, and structural deterioration, which hinder their practical application. Therefore, a mechanistic understanding of the cationic/anionic redox activity and capacity fading is indispensable for the further improvement of electrochemical performance. Here, a prototype cathode material of P2-type $Na_{0.6}Mg_{0.3}Mn_{0.7}O_2$ is comprehensively investigated, which presents both cationic and anionic redox behaviors during the cycling process. By a combination of soft X-ray absorption spectroscopy and electroanalytical methods, we unambiguously reveal that only oxygen redox reaction is involved in the initial charge process, then both oxygen and manganese participate in the charge compensation in the following discharge process. In addition, a gradient distribution of Mn valence state from surface to bulk is disclosed, which could be mainly related to the irreversible oxygen activity during the charge process. Furthermore, we find that the average oxidation state of Mn is reduced upon extended cycles, leading to the noticeable capacity fading. Our results provide deeper insights into the intrinsic cationic/anionic redox mechanism of P2-type materials, which is vital for the rational design and optimization of advanced cathode materials for SIBs.

Keywords: sodium-ion batteries; P2-tpye oxides; charge compensation mechanism; X-ray absorption spectroscopy; electronic structure

1. Introduction

The rapid development of electronic devices and electric vehicles calls for electrochemical energy storage with an ever-increasing energy density. At the moment, lithium-ion batteries (LIBs) are dominating the market because of their high operating voltages and superior energy densities [1]. However, lithium availability exhaustion and rising costs have driven researchers to explore suitable

alternatives. From this point of view, sodium-ion batteries (SIBs) are the prospective candidates of the next-generation "beyond-lithium-ion" batteries because of the natural abundance of sodium resources and the similar chemical properties of sodium and lithium [2,3].

So far, significant efforts have been devoted to find suitable cathode materials with desired properties and outstanding electrochemical performance for SIBs. Generally, the cathode materials can be mainly categorized into three groups: layered transition metal oxides (Na_xTMO_2, transition metal denotes as TM), polyanionic types and Prussian blue derivates [4–6]. Among them, layered Na_xTMO_2 has been intensively investigated in terms of their high specific capacity, convenient synthesis process and simple structure [6]. According to the occupied sites of Na^+ and the stacking sequence of oxygen layers, the layered Na_xTMO_2 materials can be further classified into two main structures: P2 phase and O3 phase [7]. Compared with O3 phase, P2 structure provides a wider diffusion path for Na^+, leading to faster ion/electron transfer rates and superior rate performances [8]. Particularly, P2-type Na_xMnO_2 has the advantages of low-cost and environmental friendliness, which make it suitable for grid-scale energy storage [9]. However, the presence of high-spin (HS) Mn^{3+} in Na_xMnO_2 can arise the Jahn-Teller (JT) distortion, which is detrimental to the structural stability. Different approaches have been proposed to alleviate this issue, such as substituting Mn with other electrochemically inactive low-valence elements (e.g., Li^+, Mg^{2+}, and Zn^{2+}) [9,10].

To further promote the specific capacity and energy density of P2-type Na_xMnO_2, anionic redox concept has been introduced as a lever to provide additional capacity [11,12]. Actually, the anionic redox chemistry has been first proposed and then widely investigated in the LIB systems [13–15]. Starting from the early chalcogenides, to the later $LiCoO_2$, then to the present Li-rich layered transition metal oxides, it is generally believed that the presence of nonbonding O-2p states causes the anionic redox activity [16–19]. Compared with LIBs, the development of anionic redox in SIBs is relatively late and the anionic redox mechanism in LIBs cannot be fully applied to SIBs. For example, unlike LIBs, anionic redox activity exists in both Na-deficient and Na-rich electrode materials of SIBs [20–22]. Therefore, a comprehensive understanding of the anionic redox in SIBs is vital to decipher the underlying electrochemical reaction mechanism, which is still elusive so far. This is mainly because most of the reported electrode materials, such as P2-$Na_{5/6}(Li_{1/4}Mn_{3/4})O_2$, P2-$Na_{0.67}(Mg_{0.2}Mn_{0.8})O_2$, contain a certain amount of Mn^{3+} ions, which participate in the charge compensation in the initial charge process and further complicate the anion redox process [23,24].

Herein, we synthesize a prototype cathode material P2-type $Na_{0.6}Mg_{0.3}Mn_{0.7}O_2$ (NaMMO) with Mg^{2+} and Mn^{4+} in the TM layers, both of which are considered to be electrochemically inactive owing to their instability under higher valence states [25]. The cationic and anionic redox behaviors and the fading mechanisms upon cycling are systematically investigated by a combination of soft X-ray absorption spectroscopy (sXAS) and electroanalytical methods. We believe the present study can provide a new avenue to design and optimize P2-type Mn-based Na_xTMO_2 material with both cationic and anionic redox activities.

2. Materials and Methods

2.1. Material Synthesis

$Na_{0.6}Mg_{0.3}Mn_{0.7}O_2$ (referred to as NMMO below) was synthesized by a traditional solid-state reaction of Na_2CO_3 (99.99%, Aladdin Reagent, Shanghai, China), $Mg(OH)_2$ (99%, Aladdin Reagent, Shanghai, China), and $MnCO_3$ (99.95%, Aladdin Reagent, Shanghai, China). The precursors weighed in the desired stoichiometric ratio were ball-milled with ethanol as dispersant for 8 h at 400 rpm, and then dried at 80 °C for 12 h in the oven. The dried powders were hand-ground using mortar and pestle and then pressed into 13 cm pellets using a press die. The pellets were calcined at 850 °C for 12 h in air and quickly cooled to room temperature using the quenching method.

2.2. Electrochemical Measurements

The electrochemical measurements were performed with CR2032 coin-type cells. The cathode electrodes were prepared by mixing NaMMO powder with acetylene black and polyvinylidene fluoride (PVDF) (8:1:1) dispersed in N-methy1-2-pyrrolidone (NMP). Then the homogeneous slurry was cast on carbon coated Al foil with a doctor blade and dried at 120 °C for 12 h under vacuum. The battery assembly was carried out in a glove box under argon atmosphere. Then sodium metal foil was used as the negative electrode and glassy fiber filter was used as the separator, and 1.0 M $NaPF_6$ in polycarbonate (PC) with fluoroethylene carbonate (FEC, 5% in volume) as the electrolyte.

2.3. Morphology and Crystal Structure Characterizations

The phase of NaMMO was investigated with lab X-ray diffraction (XRD; Empyrean, Malvern Panalytical, Almelo, Netherlands) using Cu Kα as the X-ray source. Rietveld refinement was conducted by the program of GSAS. The morphology of the samples was examined by a scanning electron microscope (SEM, G500, Zeiss, Oberkochen, Germany). High resolution lattice stripes and EDS maps of the samples were obtained by transmission electron microscopy (TEM, 200X, Talos, Thermo Fisher Scientific, Waltham, MA, USA).

2.4. Soft X-ray Experiments

The electrodes charged/discharged to the selected states of charge were disassembled carefully and cleaned repeatedly with dimethyl carbonate (DMC) to remove the residual carbonate and other impurities on the surface. Then the cleaned electrodes are put into the transition chamber and vacuum dried and stored in an argon atmosphere.

The sample to be tested is transferred into the load lock chamber through a specially designed glove box and evacuated. After that, it was transferred to the analysis chamber for testing under ultra-high vacuum. The soft X-ray absorption spectra (sXAS) in TFY and TEY mode were normalized by a gold mesh in the end station.

3. Results

The as-prepared NaMMO cathode was synthesized by a traditional solid-state method and its crystal structure was studied by the powder X-ray diffraction (XRD). The XRD patterns are highly consistent with the corresponding Rietveld refinement results as shown in Figure 1a, indicating that NaMMO is well-indexed to the pure P2 phase with a space group $P6_3/mmc$. It should be noted that the diffraction peak (enlarged view in Figure 1a) located at 2θ around 21° is not related to the space group $P6_3/mmc$ but to the $\sqrt{3}a \times \sqrt{3}a$-type supercell, implying the existence of long-range Mg^{2+}/Mn^{4+} cationic honeycomb ordering within the TM layers [26]. The corresponding crystal structure of NaMMO is depicted in Figure 1b,c, which is composed of alternate TMO_6 layers and Na^+ layers in the z-direction. Specifically, the oxygen layers stack with the ABBA sequence, in which the cations orderly distribute in the form of honeycomb-type as aforementioned to minimize the electrostatic energy [27]. In addition, there are two types of Na^+ sites situated between the TMO_6 slabs: one sharing two faces with the TMO_6 slabs, called Naf; the other sharing six edges with the TMO_6 slabs, called Nae.

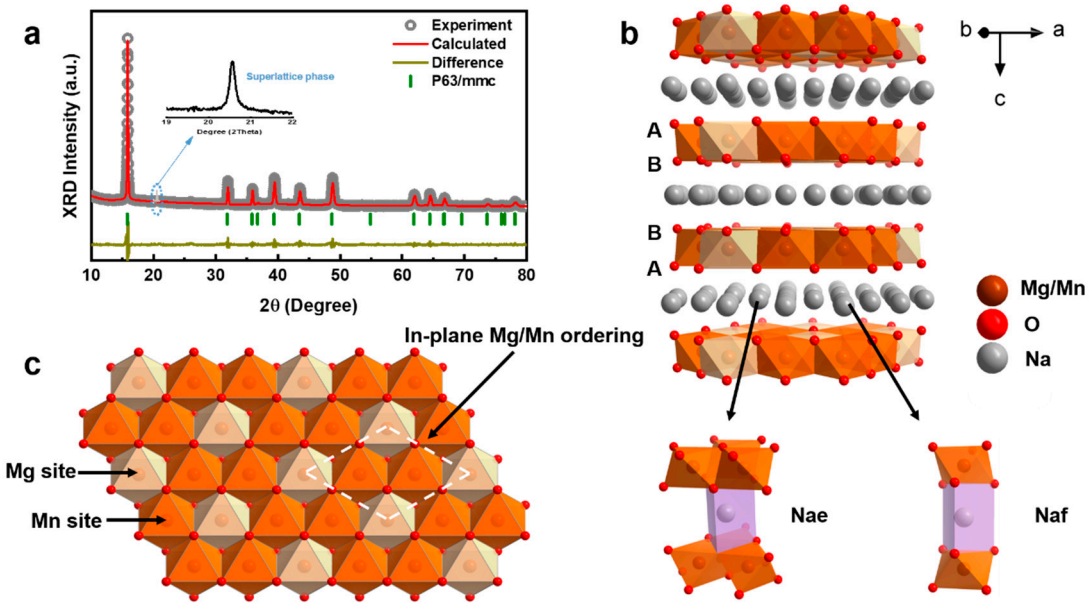

Figure 1. (**a**) XRD patterns and Rietveld refinement curves of NaMMO. The insert shows the enlarged view at 2θ between 19°–22°. (**b**) Schematic diagram of the crystal structure. (**c**) Mg^{2+}/Mn^{4+} cationic honeycomb ordering in the TM layers, viewed along the z directions.

The scanning electron microscopy (SEM) images of as-synthesized NaMMO, displayed in Figure 2a,b, exhibit a plate-like layered structure with a lateral size of ~1 μm. The high-resolution transmission electron microscope (HRTEM) image depicted in Figure 2c shows the distinct lattice fringes, suggesting the high crystallinity of NaMMO. In addition, the interplanar spacing is 4.75 Å, which corresponds to the (200) plane. This is consistent with the Rietveld refinement results discussed above, further confirming the highly crystalline P2-type structure of NaMMO. Furthermore, the uniform distribution of Na, Mg, Mn and O elements in the particles is evidenced by the corresponding energy-dispersive spectrometry (EDS), as shown in Figure 2d–h. Overall, these results unambiguously confirm the successful synthesis of P2-type NaMMO with high crystallinity.

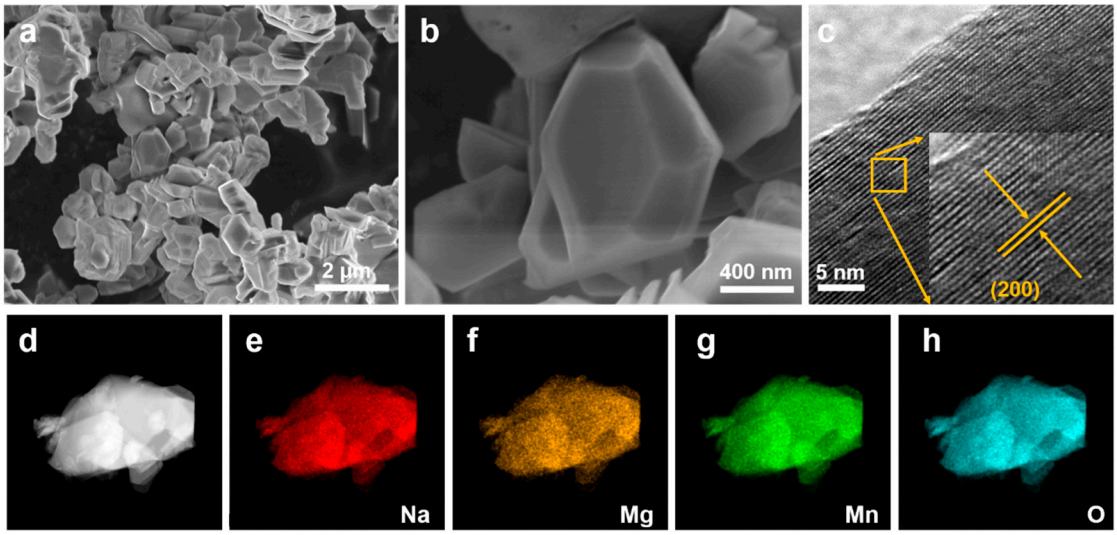

Figure 2. (**a**,**b**) SEM images of NaMMO particles. (**c**) HRTEM images at the (200) zone axis. (**d**–**h**) EDS mappings.

The electrochemical performance of the NaMMO electrode was systematically investigated using Na half cells with 1.0 M $NaPF_6$ in propylene carbonate (PC) with fluoroethylene carbonate (FEC, 5% in

volume) as the electrolyte. The galvanostatic charge/discharge curve of the first cycle in the voltage range of 1.5–4.5 V at a rate of 0.05 C is displayed in Figure 3a. The initial specific charge capacity reaches 154 mAh/g with a very long plateau at ~4.2 V, corresponding to the strong peak at the high voltage region shown in the dQ/dV curve shown in Figure 3c. Considering that tetravalent manganese cannot be further oxidized in the set voltage range, the long plateau at ~4.2 V suggests that oxygen is involved in the charge compensation process during the first charge process.

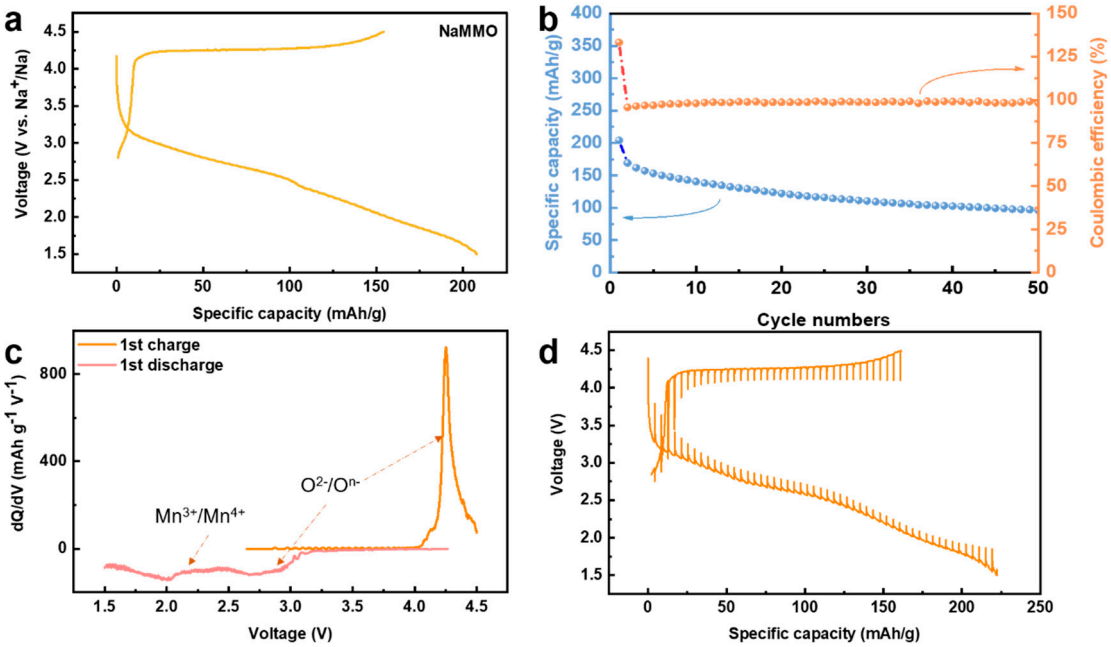

Figure 3. (**a**) Galvanostatic charge/discharge profiles of NaMMO for the 1st cycle at C/20 between 4.5 and 1.5 V vs. Na^+/Na. (**b**) Cycle performance at C/20 between 4.5 and 1.5 V. (**c**) dQ/dV plots for the 1st cycle. (**d**) The GITT curves for the 1st cycle.

It is noteworthy that different from the first charge profile, the following discharge profile presents a long slope, suggesting the relatively large voltage hysteresis. This can be seen more intuitively in the differential capacity curve (Figure 3c), which shows a reduction peak at 2.75 V, corresponding to the oxygen reduction. Note that this reduction peak is about 1.5 V away from the oxidation peak of 4.25 V. This strong voltage hysteresis could be associated with the intrinsic property of oxygen redox, and/or the honeycomb superstructure ordering in the TM layers, as reported recently [28,29]. Note that the assignment of redox peaks using dQ/dV curve has been widely applied for Mn-based sodium layered transition metal oxide cathodes for SIBs, and the Mn redox potential is usually lower than 2.5 V [28,29].

In addition, the attribution of the feature at 2 V to the Mn reduction is mainly based on the dramatic decrease of the Mn oxidation state after discharging to lower voltage range below 2.5 V, as discussed below, so in addition to the oxygen reduction peak, another reduction peak occurs at ~2 V, corresponding to the reduction of manganese. In other words, unlike the charge process where only oxygen is oxidized, both oxygen and manganese are involved in the reduction process during the discharge process. The NaMMO electrode delivers an initial discharge capacity of 207 mAh g^{-1} in the voltage range of 1.5–4.5 V at 0.05 C, and a capacity retention of 50% is achieved after 50 cycles. The galvanostatic intermittent titration technique (GITT) was further performed to investigate the diffusion kinetics of this cathode material (Figure 3d). A quasi-open circuit voltage (QOCV) of the long voltage plateau is 4.12 V, suggesting the relatively poor kinetics. The inferior capacity retentions and sluggish kinetics are probably related to the irreversible oxygen activity and electrode/electrolyte interface side reactions as discussed below.

The above results clearly indicate that the charge capacity of the first cycle mainly originates from the oxidation of oxygen. In order to understand the contributions of oxygen and manganese reduction to the discharge capacity, controllable charge/discharge profiles were obtained by controlling the charging time [30]. As shown in Figure 4a, with increasing the charging time from 5 h to 20 h, the charge capacity continuously increases from 42 mAh/g to 170 mAh/g accompanied by the growth of the discharge capacity above 2 V. By setting specific cut-off voltages to exactly match the discharge capacity with the charge capacity, it is found that these cut-off voltages vary around a small range (1.96 to 2.17 V), which may result from irreversible oxygen activity and structural distortion during the charge process. This part of the released oxygen cannot be reduced during discharge, so certain manganese is required to participate in the charge compensation mechanism to provide capacity, causing a slight decrease in the low cut-off voltage. Similar phenomenon has also been observed for the electrode material $Na_{2/3}Mg_{1/3}Mn_{2/3}O_2$ [30]. Interestingly, in addition to the growth of the discharge capacity above 2 V, with the increase of charging time, the dQ/dV curve of the corresponding discharge curve (Figure 4b and Figure S1 in Supplementary Materials) also shows a continuous increase of the oxygen reduction peak at ~2.75 V, explicitly revealing that the discharge capacity above 2 V is mainly provided by oxygen reduction.

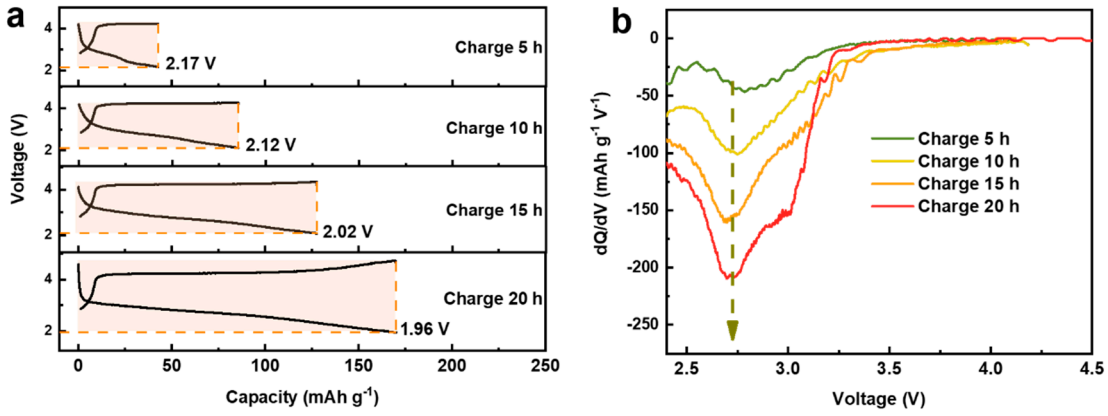

Figure 4. (**a**) The controllable charge/discharge curve as a function of charging time. (**b**) The dQ/dV curves for the corresponding discharge curves.

To further investigate the charge compensation mechanism of P2-type NaMMO upon sodiation/desodiation, we used soft X-ray absorption spectroscopy (sXAS) for NaMMO electrodes at different states of charge (SOCs) using the surface-sensitive total electron yield (TEY) mode and bulk-sensitive total fluorescence yield (TFY) mode.

Mn L-edge sXAS spectra are first measured to elucidate the valence state evolution of manganese as a function of SOCs. Note that TM K-edge hard XAS (hXAS) has been widely applied to electrode materials for exploring the oxidation states of different metal elements. However, the K-edge corresponds to the 1s-np transitions, which cannot effectively fingerprint the TM valence states (i.e., d states). In contrast, because of the dipole-allowed excitations from 2p to nd states, TM L-edge sXAS can directly probe the empty d orbitals, which are extremely sensitive to the formal valence states of TMs [31–33].

Figure 5a shows the Mn L-edge sXAS of NaMMO at different SOCs of the first cycle. In general, there are mainly two features located at 638–643 eV and 649–657 eV, which are assigned to the L_3 (Mn $2p_{3/2}$ to Mn 3d transition) and L_2 edges (Mn $2p_{1/2}$ to Mn 3d transition), respectively. Note that the $2p_{1/2}$ core hole has a shorter lifetime, leading to a broad feature for L_2 edges [34], and therefore, we will mainly focus on the Mn L_3-edge features in the following discussions.

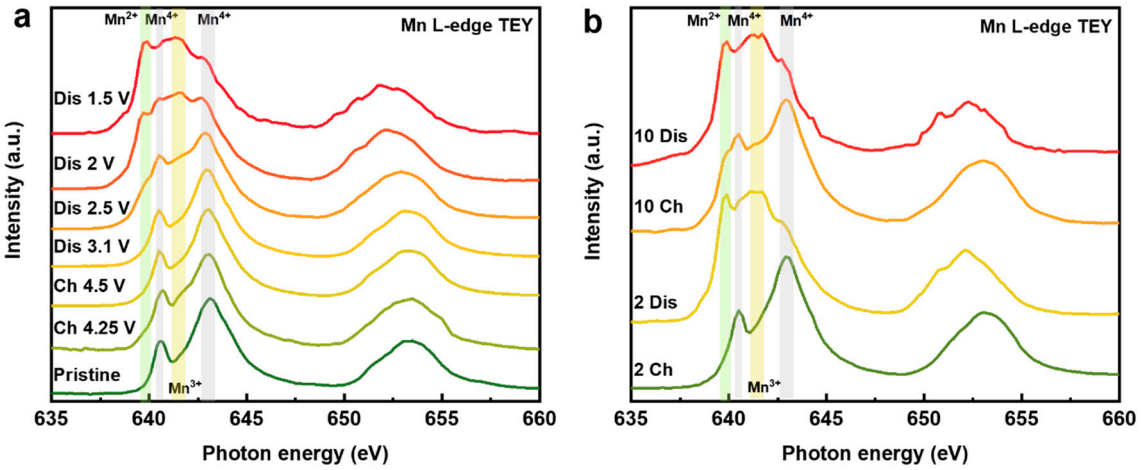

Figure 5. Mn L-edge sXAS (TEY mode) collected at different SOCs of the initial cycle (**a**) and at fully charged and discharged states after 2 and 10 cycles (**b**).

For the spectrum of pristine electrode, it exhibits an obvious Mn^{4+} feature with two well-defined peaks at 640.3 and 642.8 eV, suggesting that the pristine electrode mainly contains Mn^{4+} as expected. Upon charging to 4.25 V, a little hump at around 642 eV appears, representing the emergence of the trace amount of Mn^{3+} on the electrode surface. This counterintuitive phenomenon could be related to the electrolyte degrades in high voltage region, which produces a surface parasitic reaction to reduce the Mn on the surface [35]. The spectral shape remains invariant with the discharge voltage above 3.1 V, indicating that manganese does not participate in the charge compensation during this part of the electrochemical process, in good accordance with the above electroanalytical measurements. With continuous discharge to 2.5 V, a weak shoulder peak at 639.9 eV related to Mn^{2+} and a broad hump at 642 eV attributed to Mn^{3+} emerge, implying the gradual reduction of Mn. When discharging to 2 V, the spectral lineshape displays a substantial difference compared with the spectrum discharged to 2.5 V. The intensities of the characteristic features of Mn^{3+} and Mn^{2+} largely increase accompanied by a further decrease of the Mn^{4+} features. At fully desodiated state (1.5 V), this trend is further strengthened by the near obliteration of the Mn^{4+} features, while the characteristic features of Mn^{2+} and Mn^{3+} reach their maxima. Obviously, the concentrations of Mn^{2+} and Mn^{3+} are much higher than that of the pristine electrode, which implies a dramatic change in the chemical environment and structure of the electrode surface after just one cycle. The high concentration of Mn^{2+} on the surface at discharged state is ascribed to the surface reaction with electrolyte and/or the surface densification induced by oxygen release, as proposed previously [36].

To further explore the surface evolution and the capacity fading mechanism of NaMMO electrode upon extended cycles, we further record the Mn L-edge TEY spectra of the fully charged/discharged electrodes after 2 and 10 cycles, as shown in Figure 5b. The spectral shape of NaMMO electrode after second charge is identical to that of the first charge, indicative of the recovery of Mn^{4+}. A similar phenomenon is also observed for NaMMO after second discharge, indicating the high reversibility of Mn redox for the first two cycles. Therefore, the capacity fading (Figure S2 in Supplementary Materials) should be mainly ascribed to the possibly irreversible oxygen activity. Interestingly, the reversibility of Mn redox decreases and the amount of Mn^{2+} on the electrode surface gradually increases after 10 cycles, as shown in Figure 5b. To better visualize the reversibility of manganese redox upon extended cycles, the spectral difference and spectral derivative for the 1st, 2nd and 10th cycles are shown in the Figure S3 (See Supplementary Materials), which demonstrate that the Mn redox reversibility is relatively high for the first two cycles compared with that of the tenth cycle. The above data indicate that the evolution of manganese valence may experience a main reversible cycling reaction ($Mn^{4+} \rightarrow Mn^{4+/3+} \leftrightarrow Mn^{3+/2+}$) followed by a progressively irreversible degradation process ($Mn^{4+} \rightarrow Mn^{2+}$, irreversible) during extended cycles. Note that the Mn^{2+} on the electrode surface may dissolve from the cathode

and deposit on the anode, which is detrimental to the battery performance [37]. Therefore, the increase of low-valence manganese is partially responsible for the decreased capacity upon extended cycling.

It should be mentioned that due to the self-absorption effect, the bulk-sensitive Mn L-edge TFY spectra are distorted, resulting in the intensity suppression of the Mn L_3-edge [38]. However, the L_2-edge features are less influenced, as shown in Figure S4 (See Supplementary Materials). We can therefore conclude the oxidation state change of bulk Mn through the shift of the L_2-edge centroid [39]. It is found that the peak centroid of NaMMO remains constant during whole initial charge process, demonstrating that Mn redox in the bulk is suppressed and only oxygen is involved in the charge compensation. With the increase of the cycle numbers, the position of the peak is gradually shifted towards lower energy region, indicating the gradual decrease of Mn oxidation state in the bulk. The Mn reduction occurs both in the bulk and on the surface of NaMMO electrodes, leading to the observed capacity fading upon extended cycles.

To further understand the interplay between the cationic redox and anionic redox for NaMMO electrodes, O K-edge XAS measurements are also conducted (Figure 6). Generally, the spectra can be divided into two regions. The pre-edge features below 535 eV correspond to the excitation from O 1s orbitals to unoccupied O 2p orbitals hybridized with Mn 3d orbitals. While the broad hump above 535 eV represents the transition from O 1s orbitals to O 2p orbitals hybridized with Mn 4s and 4p orbitals. Obviously, two pre-edge features centered at 529.5 eV and 531.5 eV are assigned to the t_{2g} and e_g states as a consequence of a combined effect of exchange energy and crystal field, respectively [40].

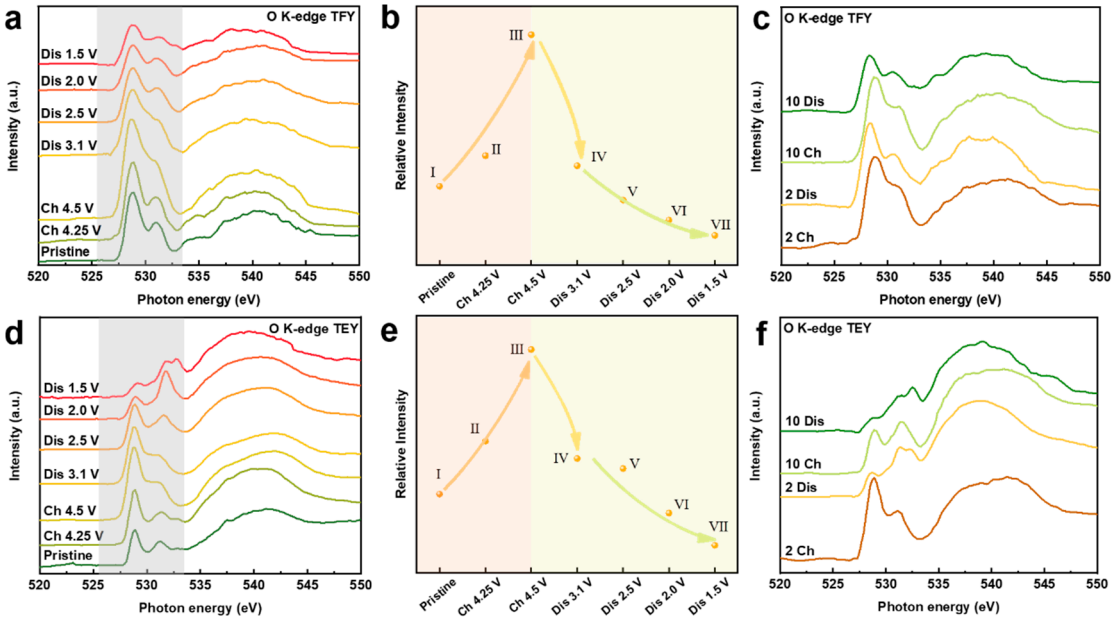

Figure 6. (**a**,**d**) O K-edge XAS spectra of NaMMO electrodes at different SOCs during the initial cycle in TEY and TFY modes, respectively. (**b**,**e**) The intensities of the pre-edge features at different SOCs during the initial cycle in TEY and TFY modes, respectively. (**c**,**f**) The O K-edge XAS spectra of NaMMO electrodes at fully charged/discharged states after 2 and 10 cycles in TEY and TFY modes, respectively.

We first discuss the pre-edge features of the bulk-sensitive TFY spectra. Note that the spectral lineshape of two pre-edge peaks is dominated by the valence states of TMs, and the integrated pre-edge intensity (525.5–533.5 eV; marked with shadow region) corresponds to the Mn-O hybridization strength [41,42]. During the first charge process, there are two main changes in this regime. Firstly, the intensity of the pre-edge features increases, indicating the hybridization between transition metal and oxygen is enhanced. Combined with the result that manganese is not involved in the redox reaction in this interval, it is very likely that the increase in hybridization strength is partly related to the influence of ligand oxygen [43]. Secondly, the dip between t_{2g} and e_g states is gradually filled. Note that mapping

of resonant inelastic X-ray scattering (mRIXS) is a powerful tool to explore the lattice oxygen redox by disentangling the intrinsic oxygen redox from the TM-O hybridization [41]. In mRIXS, the lattice oxygen redox can be confirmed through the emergence of a specific feature at 531 eV excitation energy and 523.7 eV emission energy [44,45]. The position of this feature lies exactly between t_{2g} and e_g features in the excitation energy coordinate system. Hence, this filled dip can indirectly indicate the presence of lattice oxygen redox during the first charge process. It should be noted that the filling of this dip may also be related to the reduction of manganese, as proposed previously [46]. However, the exact explanation for this phenomenon remains ambiguously, which will be investigated in detail for our future study.

Upon subsequent discharge to 2.5 V, the integrated intensity decreases continuously, with the reappearance of the dip between t_{2g} and e_g states. In combination with the Mn L_2-edge TFY spectra and the electrochemical analysis discussed above, the reappearance of the dip should be related to the reduction of oxygen in this voltage regime. The further decrease of the pre-edge intensity after discharge to 1.5 V is related to the reduction of Mn and thus the decreased hybridization strength between Mn and O, in good accordance with the downward shift of the peak centroid of Mn L_2-edge.

The spectral evolution of O K-edge XAS in TEY mode shows a similar trend as that in TFY mode. For the TEY results, the slope from point I to point II is higher than that of the TFY results, which is related to the surface activity at charged state. More specifically, after discharge to 2 V, the intensity ratio of t_{2g} and e_g states (t_{2g}/e_g) dramatically decreases as a consequence of electron filling into the t_{2g} energy level. The different t_{2g}/e_g ratios between bulk and surface once again suggest that manganese is more reduced on the electrode surface compared with that in the bulk, indicating a gradient distribution of the valence state of Mn from the surface to the bulk. This phenomenon is related to the surface densification and/or the surface side reaction with organic electrolyte and the formation of oxygen vacancies on the surface of the cycled electrode due to the irreversible oxygen activity, which has been reported for the related Na-deficient SIB cathodes and Li-excess LIB cathodes [8,33,43]. The pre-edge intensity is continuously reduced after 2 and 10 cycles, further demonstrating the continuous reduction of Mn as the cycle number increases, which leads to the inferior electrochemical performance upon extended cycling.

4. Conclusions

In summary, we have successfully designed and synthesized P2-type NaMMO electrode materials for advanced SIBs. The charge compensation and capacity fading mechanisms of NaMMO have been systematically investigated by a combination of sXAS and electroanalytical methods. The results provide solid evidence that the initial charge capacity is solely provided by the anion oxidation, leading to a long charge voltage plateau. While for the following discharge process, the capacity from the high voltage region is provided by anion reduction, and the capacity is mainly contributed by manganese reduction at the low voltage region. Combined with the surface-sensitive and bulk-sensitive sXAS spectra, a gradient distribution of Mn valence states from the surface to the bulk of the cycled electrodes is disclosed, which is highly associated with the irreversible oxygen activity and surface reaction with electrolyte. A decrease in the average valence of Mn upon extended cycles, which may be caused by irreversible oxygen activity, is observed, which results in gradual capacity fading. We believe that this work can provide a better understanding of cationic and anionic redox behaviors in Na-deficient layered cathodes, which may offer a promising perspective for developing high-performance P2-type cathode materials for SIBs.

Supplementary Materials: The following are available online at http://www.mdpi.com/1996-1073/13/21/5729/s1, Figure S1: The dQ/dV curves for the corresponding charge/discharge curves as a function of charging time. Figure S2: charge/discharge curves for the first two cycles at C/20 between 4.5 and 1.5 V (vs. Na+/Na). Figure S3: (a) The spectral difference between Mn L-edge TEY of 1 Ch 4.5 V and that of 2 Ch 4.5 V. (b) The spectral difference between Mn L-edge TEY of 1 Ch 4.5 V and that of 10 Ch 4.5 V. (c) The spectral derivative of 1 Ch 4.5 V, 2 Ch 4.5 V and 10 Ch 4.5 V, respectively. Figure S4: (a) The Mn L-edge XAS spectra (TFY mode) collected on NaMMO

electrodes as a function of SOCs during the initial cycle. (b) The Mn L-edge XAS spectra (TFY mode) collected on NaMMO electrodes as a function of SOCs after 5 and 10 cycles.

Author Contributions: C.C. designed and performed the experiments; C.C. wrote the original manuscript; C.C., N.Z. and T.Y. conceived the XAS measurement; M.D., J.M. and K.D. contributed to the discussion and analysis on the XAS results; L.Z. and J.G. revised the paper and supervised the work. All authors have read and agreed to the published version of the manuscript.

Funding: This research received no external funding.

Acknowledgments: This work is supported by Collaborative Innovation Center of Suzhou Nano Science & Technology, the Priority Academic Program Development of Jiangsu Higher Education Institutions (PAPD), the 111 project, Joint International Research Laboratory of Carbon-Based Functional Materials and Devices, the National Natural Science Foundation of China (11905154), the Natural Science Foundation of the Jiangsu Higher Education Institutions of China (19KJA550004), the Natural Science Foundation of Jiangsu Province (BK20190814). The authors thank SSRF (beamline 02B02) TLS (beamline 20A) and NSRL (beamline 11U) for the allocation of synchrotron beamtime.

Conflicts of Interest: The authors declare no conflict of interest.

References

1. Nitta, N.; Wu, F.; Lee, J.T.; Yushin, G. Li-ion battery materials: Present and future. *Mater. Today* **2015**, *18*, 252–264. [CrossRef]
2. Yu, L.; Wang, L.P.; Liao, H.; Wang, J.; Feng, Z.; Lev, O.; Loo, J.S.C.; Sougrati, M.T.; Xu, Z.J. Understanding fundamentals and reaction mechanisms of electrode materials for Na-ion batteries. *Small* **2018**, *14*, 1703338. [CrossRef]
3. Pan, H.; Hu, Y.-S.; Chen, L. Room-temperature stationary sodium-ion batteries for large-scale electric energy storage. *Energy Environ. Sci.* **2013**, *6*, 2338–2360. [CrossRef]
4. Brant, W.R.; Mogensen, R.; Colbin, S.; Ojwang, D.O.; Schmid, S.; Häggström, L.; Ericsson, T.; Jaworski, A.; Pell, A.J.; Younesi, R. Selective control of composition in prussian white for enhanced material properties. *Chem. Matter.* **2019**, *31*, 7203–7211. [CrossRef]
5. Chen, M.; Liu, Q.; Wang, S.-W.; Wang, E.; Guo, X.; Chou, S.-L. High-abundance and low-cost metal-based cathode materials for Sodium-ion batteries: Problems, progress, and key technologies. *Adv. Energy Mater.* **2019**, *9*, 1803609. [CrossRef]
6. Liu, Q.; Hu, Z.; Chen, M.; Zou, C.; Jin, H.; Wang, S.; Chou, S.-L.; Liu, Y.; Dou, S.-X. The cathode choice for commercialization of Sodium-ion batteries: Layered transition metal oxides versus prussian blue analogs. *Adv. Funct. Mater.* **2020**, *30*, 1909530. [CrossRef]
7. Han, M.H.; Gonzalo, E.; Singh, G.; Rojo, T. A comprehensive review of sodium layered oxides: Powerful cathodes for Na-ion batteries. *Energy Environ. Sci.* **2015**, *8*, 81–102. [CrossRef]
8. Ma, C.; Alvarado, J.; Xu, J.; Clément, R.J.; Kodur, M.; Tong, W.; Grey, C.P.; Meng, Y.S. Exploring oxygen activity in the high energy P2-type $Na_{0.78}Ni_{0.23}Mn_{0.69}O_2$ cathode material for Na-ion batteries. *J. Am. Chem. Soc.* **2017**, *139*, 4835–4845. [CrossRef]
9. Chen, M.; Wang, E.; Liu, Q.; Guo, X.; Chen, W.; Chou, S.-L.; Dou, S.-X. Recent progress on iron- and manganese-based anodes for sodium-ion and potassium-ion batteries. *Energy Stor. Mater.* **2019**, *19*, 163–178. [CrossRef]
10. Billaud, J.; Singh, G.; Armstrong, A.R.; Gonzalo, E.; Roddatis, V.; Armand, M.; Rojo, T.; Bruce, P.G. $Na_{0.67}Mn_{1-x}Mg_xO_2$ ($0 \leq x \leq 0.2$): A high capacity cathode for sodium-ion batteries. *Energy Environ. Sci.* **2014**, *7*, 1387–1391. [CrossRef]
11. Wang, P.-F.; You, Y.; Yin, Y.-X.; Guo, Y.-G. Layered oxide cathodes for sodium-ion batteries: Phase transition, air stability, and performance. *Adv. Energy Mater.* **2018**, *8*, 1701912. [CrossRef]
12. Lee, W.; Yun, S.; Li, H.; Kim, J.; Lee, H.; Kwon, K.; Lee, J.Y.; Choi, Y.-M.; Yoon, W.-S. Anionic redox chemistry as a clue for understanding the structural behavior in layered cathode materials. *Small* **2020**, *16*, 1905875. [CrossRef] [PubMed]
13. Ceder, G.; Chiang, Y.M.; Sadoway, D.R.; Aydinol, M.K.; Jang, Y.I.; Huang, B. Identification of cathode materials for lithium batteries guided by first-principles calculations. *Nature* **1998**, *392*, 694–696. [CrossRef]

14. Sathiya, M.; Rousse, G.; Ramesha, K.; Laisa, C.P.; Vezin, H.; Sougrati, M.T.; Doublet, M.L.; Foix, D.; Gonbeau, D.; Walker, W.; et al. Reversible anionic redox chemistry in high-capacity layered-oxide electrodes. *Nat. Mater.* **2013**, *12*, 827–835. [CrossRef] [PubMed]
15. Lu, Z.; Dahn, J.R. Understanding the anomalous capacity of Li/Li[$Ni_xLi_{(1/3-2x/3)}Mn_{(2/3-x/3)}O_2$ cells using in situ X-ray diffraction and electrochemical studies. *J. Electrochem. Soc.* **2002**, *149*, A815. [CrossRef]
16. Ben Yahia, M.; Vergnet, J.; Saubanère, M.; Doublet, M.-L. Unified picture of anionic redox in Li/Na-ion batteries. *Nat. Mater.* **2019**, *18*, 496–502. [CrossRef]
17. Qiu, B.; Zhang, M.; Xia, Y.; Liu, Z.; Meng, Y.S. Understanding and controlling anionic electrochemical activity in high-capacity oxides for next generation Li-ion batteries. *Chem. Matter.* **2017**, *29*, 908–915. [CrossRef]
18. Luo, K.; Roberts, M.R.; Hao, R.; Guerrini, N.; Pickup, D.M.; Liu, Y.-S.; Edström, K.; Guo, J.; Chadwick, A.V.; Duda, L.C.; et al. Charge-compensation in 3d-transition-metal-oxide intercalation cathodes through the generation of localized electron holes on oxygen. *Nat. Chem.* **2016**, *8*, 684–691. [CrossRef]
19. Luo, K.; Roberts, M.R.; Guerrini, N.; Tapia-Ruiz, N.; Hao, R.; Massel, F.; Pickup, D.M.; Ramos, S.; Liu, Y.-S.; Guo, J.; et al. Anion Redox Chemistry in the Cobalt Free 3d Transition Metal Oxide Intercalation Electrode $Li[Li_{0.2}Ni_{0.2}Mn_{0.6}]O_2$. *J. Am. Chem. Soc.* **2016**, *138*, 11211–11218. [CrossRef] [PubMed]
20. Mortemard de Boisse, B.; Liu, G.; Ma, J.; Nishimura, S.-I.; Chung, S.-C.; Kiuchi, H.; Harada, Y.; Kikkawa, J.; Kobayashi, Y.; Okubo, M.; et al. Intermediate honeycomb ordering to trigger oxygen redox chemistry in layered battery electrode. *Nat. Commun.* **2016**, *7*, 11397. [CrossRef]
21. Yabuuchi, N.; Hara, R.; Kubota, K.; Paulsen, J.; Kumakura, S.; Komaba, S. A new electrode material for rechargeable sodium batteries: P2-type $Na_{2/3}[Mg_{0.28}Mn_{0.72}]O_2$ with anomalously high reversible capacity. *J. Mater. Chem. A* **2014**, *2*, 16851–16855. [CrossRef]
22. Maitra, U.; House, R.A.; Somerville, J.W.; Tapia-Ruiz, N.; Lozano, J.G.; Guerrini, N.; Hao, R.; Luo, K.; Jin, L.; Perez-Osorio, M.A.; et al. Oxygen redox chemistry without excess alkali-metal ions in $Na_{2/3}[Mg_{0.28}Mn_{0.72}]O_2$. *Nature Chem.* **2018**, *10*, 288–295. [CrossRef] [PubMed]
23. Yabuuchi, N.; Hara, R.; Kajiyama, M.; Kubota, K.; Ishigaki, T.; Hoshikawa, A.; Komaba, S. New O2/P2-type Li-excess layered manganese oxides as promising multi-functional electrode materials for rechargeable Li/Na batteries. *Adv. Energy Mater.* **2014**, *4*, 1301453. [CrossRef]
24. Sharma, N.; Tapia-Ruiz, N.; Singh, G.; Armstrong, A.R.; Pramudita, J.C.; Brand, H.E.A.; Billaud, J.; Bruce, P.G.; Rojo, T. Rate dependent performance related to crystal structure evolution of $Na_{0.67}Mn_{0.8}Mg_{0.2}O_2$ in a sodium-ion battery. *Chem. Matter.* **2015**, *27*, 6976–6986. [CrossRef]
25. Rong, X.; Lu, D.; Kong, X.; Geng, J.; Wang, Y.; Shi, F.; Duan, C.K.; Du, J. Harnessing the power of quantum systems based on spin magnetic resonance: From ensembles to single spins. *Adv. Phys. X* **2017**, *2*, 125–168. [CrossRef]
26. Wang, P.-F.; Guo, Y.-J.; Duan, H.; Zuo, T.-T.; Hu, E.; Attenkofer, K.; Li, H.; Zhao, X.S.; Yin, Y.-X.; Yu, X.; et al. Honeycomb-ordered $Na_3Ni_{1.5}M_{0.5}BiO_6$ (M = Ni, Cu, Mg, Zn) as high-voltage layered cathodes for sodium-ion batteries. *ACS Energy Lett.* **2017**, *2*, 2715–2722. [CrossRef]
27. Zhao, E.; Zhang, M.; Wang, X.; Hu, E.; Liu, J.; Yu, X.; Olguin, M.; Wynn, T.A.; Meng, Y.S.; Page, K.; et al. Local structure adaptability through multi cations for oxygen redox accommodation in Li-Rich layered oxides. *Energy Stor. Mater.* **2020**, *24*, 384–393. [CrossRef]
28. Dai, K.; Mao, J.; Zhuo, Z.; Feng, Y.; Mao, W.; Ai, G.; Pan, F.; Chuang, Y.-d.; Liu, G.; Yang, W. Negligible voltage hysteresis with strong anionic redox in conventional battery electrode. *Nano Energy* **2020**, *74*, 104831. [CrossRef]
29. House, R.A.; Maitra, U.; Pérez-Osorio, M.A.; Lozano, J.G.; Jin, L.; Somerville, J.W.; Duda, L.C.; Nag, A.; Walters, A.; Zhou, K.-J.; et al. Superstructure control of first-cycle voltage hysteresis in oxygen-redox cathodes. *Nature* **2020**, *577*, 502–508. [CrossRef] [PubMed]
30. Song, B.; Hu, E.; Liu, J.; Zhang, Y.; Yang, X.-Q.; Nanda, J.; Huq, A.; Page, K. A novel P3-type $Na_{2/3}Mg_{1/3}Mn_{2/3}O_2$ as high capacity sodium-ion cathode using reversible oxygen redox. *J. Mater. Chem. A* **2019**, *7*, 1491–1498. [CrossRef]
31. Gilbert, B.; Frazer, B.H.; Belz, A.; Conrad, P.G.; Nealson, K.H.; Haskel, D.; Lang, J.C.; Srajer, G.; De Stasio, G. Multiple scattering calculations of bonding and X-ray absorption spectroscopy of manganese oxides. *J. Phys. Chem. A* **2003**, *107*, 2839–2847. [CrossRef]

32. Yoon, W.-S.; Chung, K.-Y.; Oh, K.-H.; Kim, K.-B. Changes in electronic structure of the electrochemically Li-ion deintercalated $LiMn_2O_4$ system investigated by soft X-ray absorption spectroscopy. *J. Power Sources* **2003**, *119–121*, 706–709. [CrossRef]
33. Cheng, C.; Li, S.; Liu, T.; Xia, Y.; Chang, L.-Y.; Yan, Y.; Ding, M.; Hu, Y.; Wu, J.; Guo, J.; et al. Elucidation of anionic and cationic redox reactions in a prototype sodium-layered oxide cathode. *ACS Appl. Mater. Interfaces* **2019**, *11*, 41304–41312. [CrossRef]
34. Ding, M.; Cheng, C.; Wei, Q.; Hu, Y.; Yan, Y.; Dai, K.; Mao, J.; Guo, J.; Zhang, L.; Mai, L. Carbon decorated $Li_3V_2(PO_4)_3$ for high-rate lithium-ion batteries: Electrochemical performance and charge compensation mechanism. *J. Energy Chem.* **2021**, *53*, 124–131. [CrossRef]
35. Qiao, R.; Wang, Y.; Olalde-Velasco, P.; Li, H.; Hu, Y.-S.; Yang, W. Direct evidence of gradient Mn(II) evolution at charged states in $LiNi_{0.5}Mn_{1.5}O_4$ electrodes with capacity fading. *J. Power Sources* **2015**, *273*, 1120–1126. [CrossRef]
36. Lee, J.; Seo, D.-H.; Balasubramanian, M.; Twu, N.; Li, X.; Ceder, G. A new class of high capacity cation-disordered oxides for rechargeable lithium batteries: Li–Ni–Ti–Mo oxides. *Energy Environ. Sci.* **2015**, *8*, 3255–3265. [CrossRef]
37. Pieczonka, N.P.W.; Liu, Z.; Lu, P.; Olson, K.L.; Moote, J.; Powell, B.R.; Kim, J.-H. Understanding transition-metal dissolution behavior in $LiNi_{0.5}Mn_{1.5}O_4$ high-voltage spinel for lithium ion batteries. *J. Phys. Chem. C* **2013**, *117*, 15947–15957. [CrossRef]
38. Achkar, A.J.; Regier, T.Z.; Wadati, H.; Kim, Y.J.; Zhang, H.; Hawthorn, D.G. Bulk sensitive x-ray absorption spectroscopy free of self-absorption effects. *Phys. Rev. B* **2011**, *83*, 081106. [CrossRef]
39. de Groot, F.M.F. Differences between L3 and L2 X-ray absorption spectra. *Phys. B Condens. Matter* **1995**, *208–209*, 15–18. [CrossRef]
40. de Groot, F.M.F.; Grioni, M.; Fuggle, J.C.; Ghijsen, J.; Sawatzky, G.A.; Petersen, H. Oxygen 1s x-ray-absorption edges of transition-metal oxides. *Phys. Rev. B* **1989**, *40*, 5715–5723. [CrossRef]
41. Yang, W.; Devereaux, T.P. Anionic and cationic redox and interfaces in batteries: Advances from soft X-ray absorption spectroscopy to resonant inelastic scattering. *J. Power Sources* **2018**, *389*, 188–197. [CrossRef]
42. Hu, Y.; Liu, T.; Cheng, C.; Yan, Y.; Ding, M.; Chan, T.-S.; Guo, J.; Zhang, L. Quantification of anionic redox chemistry in a prototype Na-Rich layered oxide. *ACS Appl. Mater. Interfaces* **2020**, *12*, 3617–3623. [CrossRef] [PubMed]
43. Dai, K.; Wu, J.; Zhuo, Z.; Li, Q.; Sallis, S.; Mao, J.; Ai, G.; Sun, C.; Li, Z.; Gent, W.E.; et al. High Reversibility of Lattice Oxygen Redox Quantified by Direct Bulk Probes of both Anionic and Cationic Redox Reactions. *Joule* **2019**, *3*, 518–541. [CrossRef]
44. Wu, J.; Zhuo, Z.; Rong, X.; Dai, K.; Lebens-H., Z.; Sallis, S.; Pan, F.; Piper, L.F.J.; Liu, G.; Chuang, Y.-D.; et al. Dissociate lattice oxygen redox reactions from capacity and voltage drops of battery electrodes. *Sci. Adv.* **2020**, *6*, eaaw3871. [CrossRef] [PubMed]
45. Li, Q.; Yao, Z.; Lee, E.; Xu, Y.; Thackeray, M.M.; Wolverton, C.; Dravid, V.P.; Wu, J. Dynamic imaging of crystalline defects in lithium-manganese oxide electrodes during electrochemical activation to high voltage. *Nat. Commun.* **2019**, *10*, 1692. [CrossRef]
46. Simonelli, L.; Sorrentino, A.; Marini, C.; Ramanan, N.; Heinis, D. Role of Manganese in Lithium- and Manganese-Rich Layered Oxides Cathodes. *J. Phys. Chem. Lett.* **2019**, *10*, 3359. [CrossRef]